*Universitat Politècnica de Catalunya*

# Spectroscopic Characterization of $Er^{3+}$, $Yb^{3+}$ Co-Doped UC Single Crystals

*The influence of host and sensitizer concentrations*

October 22, 2018

Federal Institute for Material Research and Testing

*Biophotonics Division 1.2*

**Supervisors:**
Dr. Christian Würth[1]
Dr. Ute Resch-Genger[1]
Dr. Crina Cojocaru[2]

David Saleta Reig[1,2,*]
[*]david.saleta@gmail.com

# Spectroscopic Characterization of $Er^{3+}$,$Yb^{3+}$ Co-Doped UC Single Crystals

**David Saleta Reig**[1,2,*]

[1] *Federal Institute for Material Research and Testing (BAM), Zweiggelände Adlershof, Richard-Willstätter-Straße 11, Berlin 12489, Germany*
[2] *Europhotonics MSc, Universitat Politècnica de Catalunya (UPC), Campus Nord, Carrer de Jordi Girona 1, Barcelona 08034, Spain*

[*] david.saleta@gmail.com

**Abstract:** The energy transfer upconversion (ETU) mechanism is known to be the most efficient route for the conversion of near infrared (NIR) light to visible emission in $Ln^{3+}$-co-doped systems. In this work, we examined these energy transfer (ET) processes in $Yb^{3+}$,$Er^{3+}$-co-doped fluoride single crystals. Because of their low phonon energy, high thermal dissipation, chemical stability and high transmission in the ultraviolet, visible, and NIR, these materials are ideal systems to study such processes. Here, we focus on the influence of the concentration of the sensitizer $Yb^{3+}$ on the optical and upconversion properties of three different fluoride hosts doped with $Yb^{3+}$ and $Er^{3+}$ as a function of excitation power density and compare direct $Ln^{3+}$-excitation and excitation in the NIR *via* ET.

## References

[1] A. Kitai. *Luminescent materials and applications*. Vol. 25. John Wiley & Sons, 2008.

[2] S. Xu, S. Huang, Q. He, and L. Wang. "Upconversion nanophosphores for bioimaging". *TrAC Trends in Analytical Chemistry* 66 (2015), pp. 72–79. DOI: 10.1016/j.trac.2014.11.014.

[3] Y. I. Park, J. H. Kim, K. T. Lee, K.-S. Jeon, H. B. Na, J. H. Yu, H. M. Kim, N. Lee, S. H. Choi, S.-I. Baik, et al. "Nonblinking and nonbleaching upconverting nanoparticles as an optical imaging nanoprobe and T1 magnetic resonance imaging contrast agent". *Advanced Materials* 21.44 (2009), pp. 4467–4471. DOI: 10.1002/adma.200901356.

[4] M. K. Mahata, H. C. Hofsäss, and U. Vetter. "Photon-upconverting materials: advances and prospects for various emerging applications". In: *Luminescence-An Outlook on the Phenomena and their Applications*. InTech, 2016.

[5] H. Dong, L.-D. Sun, and C.-H. Yan. "Energy transfer in lanthanide upconversion studies for extended optical applications". *Chemical Society Reviews* 44.6 (2015), pp. 1608–1634. DOI: 10.1039/C4CS00188E.

[6] J. M. Meruga, A. Baride, W. Cross, J. J. Kellar, and P. S. May. "Red-green-blue printing using luminescence-upconversion inks". *Journal of Materials Chemistry C* 2.12 (2014), pp. 2221–2227. DOI: 10.1039/C3TC32233E.

[7] S. Baluschev, T. Miteva, V. Yakutkin, G. Nelles, A. Yasuda, and G. Wegner. "Up-conversion fluorescence: noncoherent excitation by sunlight". *Physical Review Letters* 97.14 (2006), p. 143903. DOI: 10.1103/PhysRevLett.97.143903.

[8] C. Xu and W. W. Webb. "Measurement of two-photon excitation cross sections of molecular fluorophores with data from 690 to 1050 nm". *JOSA B* 13.3 (1996), pp. 481–491. DOI: 10.1364/JOSAB.13.000481.

[9] S. Pollack and D. Chang. "Ion-pair upconversion pumped laser emission in $Er^{3+}$ ions in YAG, YLF, $SrF_2$, and $CaF_2$ crystals". *Journal of Applied Physics* 64.6 (1988), pp. 2885–2893. DOI: 10.1063/1.341572.

[10] F. Auzel. "Compteur quantique par transfert d'energie entre deux ions de terres rares dans un tungstate mixte et dans un verre". *CR Acad. Sci. Paris* 262 (1966), pp. 1016–1019.

[11] S. Fischer, N. D. Bronstein, J. K. Swabeck, E. M. Chan, and A. P. Alivisatos. "Precise Tuning of Surface Quenching for Luminescence Enhancement in CoreShell Lanthanide-Doped Nanocrystals". *Nano Letters* 16.11 (2016), pp. 7241–7247. DOI: 10.1021/acs.nanolett.6b03683.

[12] J. Zhou, Q. Liu, W. Feng, Y. Sun, and F. Li. "Upconversion luminescent materials: advances and applications". *Chemical reviews* 115.1 (2014), pp. 395–465. DOI: 10.1021/cr400478f.

[13] Y. Zhang, J. Xu, and B. Lu. "Spectroscopic properties of $Dy^{3+}$: $Bi_4Si_3O_{12}$ single crystal". *Journal of Alloys and Compounds* 582 (2014), pp. 635–639. DOI: 10.1016/j.jallcom.2013.08.090.

[14] M. J. Weber. "Radiative and Multiphonon Relaxation of Rare-Earth Ions in $Y_2O_3$". *Phys. Rev.* 171.2 (1968), pp. 283–291. DOI: 10.1103/PhysRev.171.283.

[15] G. Buse, E. Preda, M. Stef, and I. Nicoara. "Influence of $Yb^{3+}$ ions on the optical properties of double-doped Er,Yb:$CaF_2$ crystals". *Physica Scripta* 83.2 (2011), p. 025604. DOI: 10.1088/0031-8949/83/02/025604.

[16] Y. Tian, R. Xu, L. Hu, and J. Zhang. "Spectroscopic properties and energy transfer process in $Er^{3+}$ doped $ZrF_4$-based fluoride glass for 2.7 μm laser materials". *Optical Materials* 34.1 (2011), pp. 308–312. DOI: 10.1016/j.optmat.2011.09.004.

[17] M. Kaiser, C. Würth, M. Kraft, I. Hyppänen, T. Soukka, and U. Resch-Genger. "Power-dependent upconversion quantum yield of $NaYF_4$: $Yb^{3+}$, $Er^{3+}$ nano-and micrometer-sized particles–measurements and simulations". *Nanoscale* 9.28 (2017), pp. 10051–10058. DOI: 10.1039/c7nr02449e.

[18] P. Villanueva-Delgado, D. Biner, and K. W. Krämer. "Judd-Ofelt analysis of β-$NaGdF_4$: $Yb^{3+}$, $Tm^{3+}$ and β-$NaGdF_4$:$Er^{3+}$ single crystals". *J. of Luminescence* 189 (2017), pp. 84–90. DOI: 10.1016/j.jlumin.2016.04.023.

[19] C. Würth, M. Kaiser, S. Wilhelm, B. Grauel, T. Hirsch, and U. Resch-Genger. "Excitation power dependent population pathways and absolute quantum yields of upconversion nanoparticles in different solvents". *Nanoscale* 9.12 (2017), pp. 4283–4294. DOI: 10.1039/C7NR00092H.

[20] M. P. Hehlen, M. G. Brik, and K. W. Krämer. "50th anniversary of the Judd–Ofelt theory: An experimentalist's view of the formalism and its application". *J. of Luminescence* 136 (2013), pp. 221–239. DOI: 10.1016/j.jlumin.2012.10.035.

[21] L. Tu, X. Liu, F. Wu, and H. Zhang. "Excitation energy migration dynamics in upconversion nanomaterials". *Chemical Society Reviews* 44.6 (2015), pp. 1331–1345. DOI: 10.1039/c4cs00168k.

[22] F. Huang, X. Liu, L. Hu, and D. Chen. "Spectroscopic properties and energy transfer parameters of $Er^{3+}$-doped fluorozirconate and oxyfluoroaluminate glasses". *Scientific reports* 4 (2014), p. 5053. DOI: 10.1038/srep05053.

[23] P. W. Bridgman. "Certain Physical Properties of Single Crystals of Tungsten, Antimony, Bismuth, Tellurium, Cadmium, Zinc, and Tin". *Proceedings of the American Academy of Arts and Sciences* 60.6 (1925), pp. 305–383. DOI: 10.2307/25130058.

[24] B. Sobolev and K. Seiranian. "Phase diagrams of systems $SrF_2$-(Y,*Ln*)$F_3$. II. Fusibility of systems and thermal behavior of phases". *Journal of Solid State Chemistry* 39.3 (1981), pp. 337–344. DOI: 10.1016/0022-4596(81)90268-1.

[25] P. Fedorov. "Systems of alkali and rare-earth metal fluorides". *Russ. J. Inorg. Chem.* 44.11 (1999), pp. 1703–1727.

[26] H. Li. "Refractive index of alkaline earth halides and its wavelength and temperature derivatives". *Journal of Physical and Chemical Reference Data* 9.1 (1980), pp. 161–290. DOI: 10.1063/1.555616.

[27] H. Li. "Refractive index of alkali halides and its wavelength and temperature derivatives". *Journal of Physical and Chemical Reference Data* 5.2 (1976), pp. 329–528. DOI: 10.1063/1.555536.

[28] C. Würth, J. Pauli, C. Lochmann, M. Spieles, and U. Resch-Genger. "Integrating Sphere Setup for the Traceable Measurement of Absolute Photoluminescence Quantum Yields in the Near Infrared". *Analytical Chemistry* 84.3 (2012), pp. 1345–1352. DOI: 10.1021/ac2021954.

[29] C. Kesavulu, K. K. Kumar, and C. Jayasankar. "Upconversion properties of $Er^{3+}$-doped oxyfluoride glass-ceramics containing $SrF_2$ nanocrystals". In: *Oxide-based Materials and Devices V*. Vol. 8987. International Society for Optics and Photonics. 2014, 89871J. DOI: 10.1117/12.2039308.

[30] H. Qin, D. Wu, J. Sathian, X. Xie, M. Ryan, and F. Xie. "Tuning the upconversion photoluminescence lifetimes of $NaYF_4$:$Yb^{3+}$,$Er^{3+}$ through lanthanide $Gd^{3+}$ doping". *Scientific Reports* 8.1 (2018), p. 12683. DOI: 10.1038/s41598-018-30983-9.

## List of Abbreviations

| | |
|---|---|
| BET | Back Energy Transfer |
| CW | Continuous Wave |
| DS | Downshifted |
| ESA | Excited-State Absorption |
| ET | Energy Transfer |
| ETU | Energy Transfer Upconversion |
| IRF | Instrument Response Function |
| JO | Judd-Ofelt |
| NIR | Near Infrared |
| NPs | Nanoparticles |
| OD | Optical Density |
| PMT | Photomultiplier Tube |
| RE | Rare-Earth |
| SNR | Signal-to-Noise Ratio |
| UC | Upconversion |

## Symbols and Units

| | | |
|---|---|---|
| $\alpha$ | Absorption coefficients | $cm^{-1}$ |
| $\sigma_{abs}$ | Absorption cross section | $cm^2$ |
| $\beta_R$ | Branching ratio | % |
| $d$ | Crystal thickness | cm |
| $a_0$ | Lattice constant | Å |
| $P$ | Excitation power density | $W/cm^2$ |
| $\mathcal{N}$ | Number density | $cm^{-3}$ |
| $N_{abs}$ | Number of absorbed photons | 1 |
| $N_{em}$ | Number of emitted photons | 1 |
| $f$ | Oscillator strength | 1 |
| $\tau$ | Radiative lifetime | ms |
| $n$ | Refractive index | 1 |
| $k$ | Slope factor | 1 |
| $A$ | Spontaneous emission rate | $s^{-1}$ |
| $\Phi_{UC}$ | UC Quantum Yield | % |

## Contents



## 1. Introduction

Luminescent materials have always attracted considerable attention due not only to their current range of applications but also to their wide potential in the fields of optical devices and biomedicine. To date, numerous luminescent materials, such as fluorescent proteins, organic dyes, metal complexes, semiconductors, noble metal nanoparticles (NPs), as well as lanthanide-doped inorganic phosphors, have been developed to pursue numerous applications [1–7]. exhibit a Stokes shifted or downshifted or down-converted emission with the emitted photons having a lower energy than the absorbed ones. Few materials posses the ability to generate anti-Stokes photoluminescence. In these cases the emitted photons have a higher energy than those used for excitation.

Two-photon absorption-based luminescence and second-harmonic generation are two kinds of anti-Stokes processes requiring high energy lasers as excitation sources. Depending on the lifteime of the excited states involved, a two photon or multiphonic process requires the simultaneous or nearly simultaneous absorption of two coherent near-infrared (NIR) photons from a pulsed laser (usually a femtosecond laser) with a high excitation power density ($\sim 10^6$ W/cm$^2$), because of the low two-photon absorption cross sections [8]. Upconversion (UC) luminescence is a distinct, non-linear anti-Stokes process, which can be achieved using low-power and incoherent excitation sources, such as continuous-wave (CW) lasers, standard xenon or halogen lamps, or even focused sunlight [7].

Three major UC mechanisms have been elucidated from the studies of macroscopic inorganic crystals [9], *i.e.* excited state absorption (ESA), energy transfer upconversion (ETU), and photon avalanche. Of these categories, ETU is known to be the most efficient UC mechanism and is less susceptible to external conditions. When a macroscopic crystal is doped simply with one rare-earth (RE) element (as an activator) at low concentration, interactions between the ions can be neglected and ESA is responsible for the UC process. When the doping concentration is increased, interactions between the centers become significant and they can no longer be treated as activators; instead, they also act as sensitizers, *i.e.* they will transfer the excited energy to other activators to assist the UC luminescence of the latter *via* an ET mechanism.

One way to improve the UC efficiency is to use different dopants as sensitizer and activator. Because the $Yb^{3+}$ ion has a simple energy scheme and a relatively large absorption cross-section in the NIR, it has been considered a potential sensitizer to enhance the upconversion emission since the 1960s [10]. The $^2F_{7/2} \rightarrow ^2F_{5/2}$ transition of $Yb^{3+}$ is conveniently resonant

with many f-f transitions of $Er^{3+}$, $Tm^{3+}$, and $Ho^{3+}$, thus facilitating efficient ET from $Yb^{3+}$ to these ions. Hence, $Yb^{3+}$ is often co-doped with $Er^{3+}$, $Tm^{3+}$, or $Ho^{3+}$ as a sensitizer to enhance UC emission (as an example, see the energy diagram in Fig. 1 for UC emissions in $Er^{3+}/Yb^{3+}$ systems). In addition to dopant, host matrix provides a platform for ETU. The host matrix determines the environment around the dopants, which influences the efficiency of the UC luminescence.

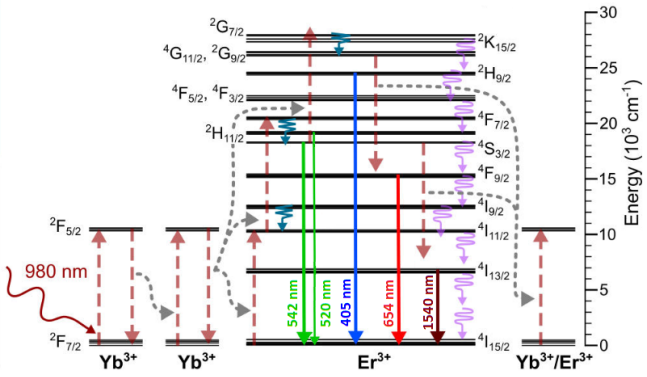


**Figure 1:** Energy scheme of $Yb^{3+}$-$Er^{3+}$ interactions responsible for upconversion and downshifted emissions under 976 nm excitation. The incident photons are predominantly absorbed by $Yb^{3+}$ and the energy is transferred to $Er^{3+}$. (Modified from Fig. 1e, [11])

Ideal host materials should have low lattice phonon energies so as to minimize non-radiative loss while favouring the radiative emission. This is because the non-radiative depopulation of excited energy states requires the assistance of phonons present in the host lattice. Heavy halides, such as chlorides, bromides and iodides generally exhibit low phonon energies (below 300 $cm^{-1}$). However, they are hygroscopic (e.g. they attract water molecules through either absorption or adsorption, affecting their properties) and are of limited use [12]. Oxides show high chemical stability, but their phonon energies are relatively high (generally larger than 500 $cm^{-1}$) [13, 14]. In comparison, fluorides usually exhibit low phonon energies ($\sim$500 $cm^{-1}$) and high chemical stability and, thus, are often used as host materials for UC processes [9, 15, 16]. To date, hexagonal β-$NaYF_4$ has been the most popular host for lanthanide UCNPs [17, 18].

Low-dimensional UC materials have gained the attention of the scientific community in recent years. As an example, $Ln^{3+}$-doped NPs have emerged as an attractive alternative to traditional bioimaging probes in the past decade [2]. Unlike organic dyes and quantum dots, they are extremely resistant to photoblinking and photobleaching even after many hours of continuous excitation [3]. In addition, NIR light does not excite the surroundings, virtually eliminating autofluorescence. Furthermore, in contrast to UV light, NIR light offers significantly better penetration depth in tissue and is less prone to scattering.

In spite of the exhaustive research carried out on UCNPs, the mechanisms behind the UC processes are not well understood [11, 19]. Macroscopic single crystals provide an ideal model system to study the UC mechanisms and interactions between RE ions in solid state. The lack of grain boundaries reduces light scattering and ensures an efficient heat dissipation. Furthermore, bulk crystals are exempt from the common complications of their NPs counterparts, such as the solvent, ligands and surface quenching effects [11, 13, 18], which play an important role in the UC efficiency and luminescence color of nanoscale systems. Therefore, macroscopic crystals are suitable systems to relate the experiments with the theory.

In this work, an extensive characterization of the optical properties of various cubic fluoride

hosts ($SrF_2$, NaF and $\alpha$-$NaYF_4$) co-doped with $Er^{3+}$ and $Yb^{3+}$ (as activator and sensitizer, respectively) has been performed as a function of the sensitizer concentration. The experimental spectroscopic data is complemented with Judd-Ofelt calculations, bringing an insight of the theoretical properties for an ideal Er-doped system while allowing for the identification of optical transitions and their characteristics in different experimental conditions. The excitation wavelength has been chosen at (*i*) 375 nm to directly pump the $^4G_{11/2}$ high energy state of $Er^{3+}$, where non-radiative relaxations are responsible for the population of its lower energy levels leading to downshifted (DS) emission; and (*ii*) 975 nm to pump the $^2F_{5/2}$ energy level of $Yb^{3+}$, where subsequent ETs populate higher excited states of $Er^{3+}$ leading to UC luminescence.

The population pathways have been studied by means of excitation spectra, where the emission intensity of a single transition is monitored as a function of the excitation wavelength. However, a complete comprehension of the processes controlling population and deactivation pathways in UC systems requires quantitative luminescence measurements including the determination of the quantum yields of the upconversion processes ($\Phi_{UC}$) and excitation power density ($P$)-dependent studies as the sequential absorption of two or more photons introduces a $P$-dependence of the UC luminescence. This renders all luminescence parameters such as emission spectra, intensity ratios of emission bands, $\Phi_{UC}$, slope factors and decay kinetics [19].

### *1.1. Judd-Ofelt Theoretical Background*

Important spectroscopic and laser parameters of RE-doped bulk materials, such as crystals and glasses, have been commonly analyzed using the Judd-Ofelt (JO) theory [20]. The great appeal of the JO theory is in its ability to predict oscillator strengths in absorption and luminescence, luminescence branching ratios, excited-state radiative lifetimes, energy-transfer probabilities, and estimates of quantum efficiencies by using only three parameters, $\Omega_{(\lambda)}$ ($\lambda = 2,4,6$). The results of the theory are accurate, in general, and confirm that the majority of transitions are due to the forced electric dipole, with some magnetic dipole contributions [18].

The UC luminescence emission of lanthanide ions rely on the f-electron configurations ($[Xe]4f^N5s^25p^6$, where $N$ runs from 1 ($Ce^{3+}$) to 13 ($Yb^{3+}$) along the series of RE ions), with abundant long lifetime ($\sim$ms) energy levels as the required intermediate excitation states. The partially filled 4f electronic shell that is critically relevant to photoluminescence is protected by outer 5s and 5p electronic shells from external environmental disturbances [21]. The weak interactions of the $RE^{3+}$ with its surroundings affect both the effective electrostatic and spin-orbit coupling strength to some extent. For a $RE^{3+}$-doped material there is, therefore, a set of electrostatic ($F_{(2)}$, $F_{(4)}$, $F_{(6)}$) and spin-orbit ($\zeta$) parameters that are characteristic for this $RE^{3+}$ and host material combination.

The energy of a 4f state $|4f^N, SLJ\rangle$ depends on the Coulomb repulsion and spin-orbit coupling between the 4f electrons, parametrized by the Slater integrals $F_{(2),(4),(6)}$ and spin-orbit parameter $\zeta$, respectively. In the intermediate coupling approximation a mixed state $|4f^N, SLJ\rangle'$ can be described as a linear combination of wavefunctions:

$$|4f^N, SLJ\rangle' = \sum c_i |4f^N, S'L'J\rangle \tag{1}$$

with coefficients $c_i$ [20]. The energy of the mixed state is then determined by the values of $F_{(2),(4),(6)}$ and $\zeta$. For a specific $RE^{3+}$-doped material it is, thus, necessary to fit these parameters to a set of experimental $^{2S+1}L_J$ multiplet energies. This yields parameters and $c_i$ coefficients appropriate to the host lattice. For a detailed explanation of the theory and the calculations of its derived quantities the reader is referred to the literature [18, 20, 22].

## 2. Experimental Methods

### 2.1. Materials

Fluoride single crystals were grown by the Bridgman technique [23] in a vacuum furnace, preliminary melting the fluoride powder precursors in a $CF_4$ fluorinating atmosphere (crystal growth was done by our collaborators from KIT). The heater and crucible were made of graphite. The growing temperature was chosen based on the phase diagrams of the host crystals (1470 °C for $SrF_2$:$REF_3$ [24], and 1000 °C for NaF:$REF_3$ [25]). The temperature gradient was set to 60 K/cm in both cases, achieving a crystallization velocities of 6.5 and 7.5 mm/h for $SrF_2$ and $\alpha$-$NaYF_4$, respectively. The growing process included the following stages: slow heating in vacuum up to the required temperature, melting of the powders, switching off the vacuum evacuation, melt fluorination by $CF_4$ and slow pulling of the crucible to the cooling zone to achieve a simultaneous crystallization.

A series of cubic single crystals $-SrF_2$ ($a_0 = 5.80$ Å), $\alpha$-$NaYF_4$ ($a_0 = 5.51$ Å) and NaF ($a_0 = 4.62$ Å), all of them with space group $Fm\bar{3}m-$ with constant 2 mol% $Er^{3+}$-doping and varying concentrations of $Yb^{3+}$ (2, 3, 5 and 7.5 mol% for $SrF_2$; 10 and 20 mol% for $NaYF_4$; and 58 mol% for NaF) were obtained. The cylindrical crystal rods with diameters below 1 cm and heights up to few cm were cut in slabs of thicknesses ($d$) between 1 and 2 mm and polished to avoid surface scattering effects for the spectroscopic inspection.

### 2.2. Instrumentation and Methods

**Steady-state absorption and fluorescence spectroscopy**

**Determination of $\sigma_{abs}$ and $f_{exp}$.** Absorption spectra were recorded at room temperature on a Cary 5000 SN spectrometer (Varian) in a transmission configuration with a wavelength step of 0.5 nm. Absorption cross sections ($\sigma_{abs}$) were calculated from the spectra such that,

$$\sigma_{abs} = \frac{\alpha}{\mathcal{N}} = \frac{OD}{d \cdot \log_{10}(e) \cdot \mathcal{N}} = \frac{2.3025 \cdot OD}{d \cdot \mathcal{N}} \tag{2}$$

where $\alpha$ is the absorption coefficient in $cm^{-1}$, $\mathcal{N}$ the number density in $cm^{-3}$, $d$ the sample thickness in cm (measured with a digital caliper), and $OD$ the optical density readily obtained from the spectrometer. Erbium absorption cross sections are used to estimate the experimental oscillator strengths, $f_{exp}$, such that,

$$\begin{aligned} f_{exp} &= \frac{4\varepsilon_0 m_e c^2}{e^2} \ln(10) \int \sigma_{abs}(\overline{\nu})\, d\overline{\nu} \\ &= 2.601 \cdot 10^{12}\ (\mathrm{cm}^{-1}) \int \sigma_{abs}(\overline{\nu})\, d\overline{\nu} \end{aligned} \tag{3}$$

where $\int \sigma_{abs}(\overline{\nu})\, d\overline{\nu}$ is the area of each absorption band (in cm) from the cross section with respect to the wavenumber. To retrieve the oscillator strength for the $Er^{3+}$:$^4I_{11/2}$ band hidden within the broad $Yb^{3+}$:$^2F_{5/2}$ manifold (see the energy diagram of $Er^{3+}$ and $Yb^{3+}$ ions in Fig. 1), we calculated the area of the peak centered at 975 nm (for $Er^{3+}$ $\sigma_{abs}(\lambda)$) for the different $SrF_2$ samples and extrapolated the area of the corresponding $Er^{3+}$ absorption band for a null contribution from $Yb^{3+}$.

**Judd-Ofelt calculations.** JO theory was implemented with the aid of RELIC software [20] (which stands for Rare Earth Level and Intensity Calculations). This software considers the wavelength-dependent refractive index $n(\lambda)$ of the host matrix by means of the six coefficients ($B_{1,2,3}$ and $C_{1,2,3}$), which were obtained from literature values for $SrF_2$ [26] and NaF [27], in the Sellmeier equation:

$$n(\lambda)^2 = 1 + \sum_{i=1}^{3} \frac{B_i \lambda^2}{\lambda^2 - C_i} \tag{4}$$

The RELIC software was used to calculate the 4f wavefunctions in the intermediate coupling approximation and fit the Slater integrals $F_{(2),(4),(6)}$ and the spin-orbit coupling parameter $\zeta$ to the experimental peak energy of the absorption bands. The starting $F_{(2),(4),(6)}$ and $\zeta$ parameters were taken as suggested in RELIC's user guide for $Er^{3+}$ ions. The three Judd-Ofelt parameters $\Omega_{2,4,6}$ were then fit to the experimental oscillator strengths. The intrinsic radiative lifetimes ($\tau_{cal}$), spontaneous emission rates ($A$), branching ratios ($\beta_R$) and, finally, the theoretical oscillator strengths ($f_{cal}$) for all possible optical transitions of $Er^{3+}$ ions were calculated.

**Downshifted emission and excitation spectra.** Both, emission and excitation spectra were measured with a calibrated spectrofluorometer FSP-920 (Edinburgh Instruments) in a depolarised excitation/detection geometry, which was equipped with a conventional continuous xenon lamp. All the spectra were measured with a 0.5 nm step. For the emission spectra, the excitation slits widths were fixed at 4 nm. Excitation scans allow us to retrieve the population dynamics of a single energy level, by probing its luminescence intensity when higher energy levels are excited. The detection slit widths for recording the excitation spectra were chosen to ensure the availability of correction files to account for the lamp's wavelength-dependent photon flux at the sample position. Hence, excitation scans were measured using 1 nm slit widths for the 542 and 980 nm emissions, and 2 nm for the 655 nm emission. In order to cover the wavelength range from 400 to 1700 nm, two different detectors −a red extended PMT (R2658P) and a NIR PMT (R5509P) from Hamamatsu− with overlapping detection windows were used.

### Time-resolved fluorescence measurements

**Luminescence decay kinetics.** Lifetime measurements were carried out with two commercial spectrofluorometers, the previously described FSP-920 and a FLS-980 (Edinburgh Instruments). The FLS-980 setup with multichannel scaling was equipped with an 8 W 976 nm laser diode (pulse width 100 µs), and the excitation power density was fixed at *ca.* 15 W/cm$^2$ for all the experiments to prevent an influence of this parameter on the measured decay kinetics/lifetime. The FSP-920 spectrofluorometer was also equipped with a µ-flash lamp 920H (pulse width 100 µs) with an excitation power density below 1 W/cm$^2$ and a red extended PMT (R2658P) from Hamamatsu. The slit widths for the excitation and detection were adjusted in every case to keep a similar photon rate (∼2000 cps) between the different samples. Pulse widths were measured from the baseline of the instrument response function (IRF).

**Data analysis.** The decay curves were normalized to one after the excitation pulse. These were analyzed with origin *via* single, double or triple exponential decay fitting curves, which were performed with a tail-fit (starting only after the excitation pulse was turned off) instead of a deconvolution procedure of the recorded decay curves with the IRF which is usually mandatory for accurate analysis of fluorescence lifetimes from time-correlated single-photon counting measurements.

### *P*-dependent upconversion parameters

**Measurement of UC luminescence.** The UC emission spectra were recorded using both, the previously described FSP-920 spectrofluorometer equipped with a 1 W 976 nm CW laser diode and a custom-designed integrating sphere setup previously described [28] and modified [17] to meet the requirements of UC luminescence measurements, such as the implementation of a high stability 8 W 976 nm laser diode as the excitation light source. The integrating sphere setup −equipped with a laser diode, a collimating and focusing optics, and a laser

clean filter, which is coupled *via* a 200 µm-sized optical fiber into a $BaSO_4$-coated integrating sphere (diameter of 15 cm) with a Si-CCD detection system– is illustrated in Fig. 2. A lense of 500 mm focal length is used to achieve a top hat beam profile at the sample position to ensure homogeneous excitation power density within the laser beam spot. Two automated filter wheels equipped with reflective neutral density filters of known transmittance sit along the excitation beam path. This allows for precise tuning of the average $P$ over four orders of magnitude, although in the present experiments the excitation power density was varied from 1 to 10 W/cm$^2$. For each emission band, the appropriate detection filter is assigned and their integration wavelength ranges are chosen to ensure spectral overlapping. The integration time for each band in each sample is adjusted to achieve the best possible signal-to-noise ratio (SNR) while avoiding detector saturation.

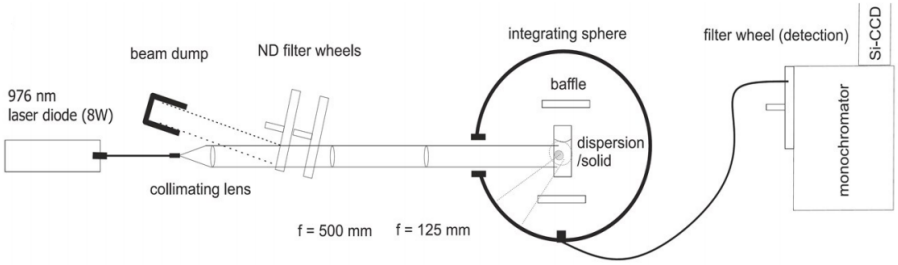


**Figure 2:** Schematic representation of the custom-designed integrating sphere setup (Fig. S1a, [17]).

***P*-dependent slope factors $k(P)$.** The slope factors were calculated from two energetically neighbouring $P$-dependent intensity values $I_{em,i}(\lambda_{em}, P_i)$ and $I_{em,j}(\lambda_{em}, P_j)$, such that

$$k(P) = \frac{\ln(I(x_j)) - \ln(I(x_i))}{\ln(x_j) - \ln(x_i)} \tag{5}$$

***P*-dependent intensity ratios.** The ratios between each of the integrated emission bands in the visible range were calculated as a function of the excitation power density from the spectra obtained in the integrating sphere setup. The intensity ratios are taken with respect to a stronger emission band in every case (*e.g.* $I_{b/g}$, $I_{g/g}$ and $I_{g/r}$) to obtain comparable values below one.

**Measurement of *P*-dependent absolute $\Phi_{UC}$.** The determination of absolute UC quantum yields ($\Phi_{UC}$) in the integrating sphere setup includes the following steps: (*i*) measurement of the transmitted incident radiant power and the UC emission spectrum of the sample (crystal contained in a quartz cuvette) and a blank (empty cuvette) under identical measurement conditions; (*ii*) data evaluation including the choice of the emission wavelength region for spectral emission correction and signal integration; and (*iii*) calculation of the upconversion quantum yield, obtained from the directly measured number of emitted photons ($N_{em}$) per number of absorbed photons ($N_{abs}$) at different $P$, such that,

$$\Phi_{UC}(P) = \frac{N_{em}}{N_{abs}}, \quad \text{for } \lambda_{em} < \lambda_{ex} \tag{6}$$

Here, only those photons emitted with $\lambda_{em} < \lambda_{ex} = 976$ nm (integration over all UC emissions between 350 and 900 nm) were considered. For the calculation of $\Phi_{UC}$ for each emission band in the visible range, the $\Phi_{UC}(P)$ were rescaled by the fraction of each integrated emission with respect to the integration over all UC emissions.

To reduce temperature effects originating from the very intense incident laser light, a delay time of 30 s was implemented between single $\Phi_{UC}$ measurements. Also, $\Phi_{UC}(P)$ was calculated in duplicate, from two measurement cycles using an increasing and then a decreasing power by means of an automated filter wheels; *i.e.* the measurement begins at maximum attenuation (for 2×OD1 filters), reaches the highest power (for 1×OD1 filter) and decreases again to the lowest power (for 2×OD1 filters), each $\Phi_{UC}$ value corresponding to a unique filter-pair combination measured two times, for increasing and decreasing $P$.

Because of the broad $Yb^{3+}$ emission at 980 nm, the number of absorbed photons $N_{abs}$ is underestimated (*i.e.* these photons are treated as incident photons from the light source) leading to an overestimation of $\Phi_{UC}$. To correct for this artefact, the emission band of $Yb^{3+}$ was added to the blank to accurately estimate the absorption and, therefore, the $\Phi_{UC}$ of the $SrF_2$ crystals. The uncorrected $\Phi_{UC}$ were down-scaled by a factor of 1.1-1.3 for $Yb^{3+}$ concentrations of 7.5-2.0 mol%, respectively, to account for $Yb^{3+}$ emission at 980 nm.

## 3. Results and Discussion

The downshifted and upconversion optical properties of a series of cubic $SrF_2$, α-$NaYF_4$ and NaF single crystals, co-doped with trivalent $Er^{3+}$ and $Yb^{3+}$ ions have been studied under different excitation power densities and wavelengths, using the instrumentation and methods described in Section 2.2. The experimental data is compared and linked to Judd-Ofelt calculations, which allow to contrast the probed properties in our doubly-doped crystals with those found for ideal, singly $Er^{3+}$-doped systems.

The absorption and DS luminescence spectra ($\lambda_{ex} = 375$ nm) are presented in Section 3.1, together with the decay kinetics and calculated lifetimes for the DS emissions of the $Yb^{3+}$:$^2F_{5/2}$ and $Er^{3+}$:$^4I_{13/2}$ (at *ca.* 1000 and 1540 nm, respectively) under laser diode and μ-flash lamp excitation at 975 nm. Radiative lifetimes were also measured under μ-flash lamp excitation at 375 nm, to retrieve information on the depopulation dynamics in $Er^{3+}$ ions. The influence of the crystal field and local environments of these optical active centers are investigated by comparing the absorption, emission and decay kinetics of the different hosts.

The UC properties of these fluoride crystals are analyzed under laser diode excitation at 976 nm and presented in Section 3.2 by means of time-resolved measurements for the green ($^2H_{11/2}$ and $^4S_{3/2}$ energy levels at *ca.* 540 nm) and red ($^4F_{9/2}$ at *ca.* 650 nm) UC emissions. This is complemented by excitation spectra for these energy levels together with the $Yb^{3+}$:$^2F_{5/2}$, to unravel the population pathways and complex $Er^{3+}$-$Yb^{3+}$ interactions in these systems. The $P$-dependent properties characteristic to the UC processes are investigated *via* luminescence measurements in a custom-built integrating sphere setup. The slope factors, intensity ratios and absolute quantum yields are presented for $SrF_2$.

### *3.1. Optical Properties*

#### 3.1.1. Absorption

From the absorption measurements of $Er^{3+}$/$Yb^{3+}$ co-doped crystal hosts, transparent within the 350-1700 nm wavelength range, 13 bands are identified as $Er^{3+}$ transitions from its ground state ($^4I_{15/2}$) to its excited states ($^4I_{13/2}$, $^4I_{11/2}$, $^4I_{9/2}$, $^4F_{9/2}$, $^4S_{3/2}$, $^2H_{11/2}$, $^4F_{7/2}$, $^4F_{5/2}$, $^4F_{3/2}$, $^2H_{9/2}$, $^4G_{11/2}$, $^4G_{9/2}$, and $^2G_{7/2}$); while $Yb^{3+}$ shows only one band corresponding to the transition from its ground state ($^2F_{7/2}$) to its $^2F_{5/2}$ excited state. The absorption cross sections ($\sigma_{abs}$) for $Er^{3+}$ and $Yb^{3+}$ transitions are presented in Fig. 3, for $SrF_2$ and α-$NaYF_4$. The differences in $\sigma_{abs}$ values between the host crystals arise from the local micro-environments felt by the dopants in each host matrix, such as the crystal field splitting of the various manifolds (*i.e.* clear for the $^4I_{13/2}$ band in Fig. 3a).

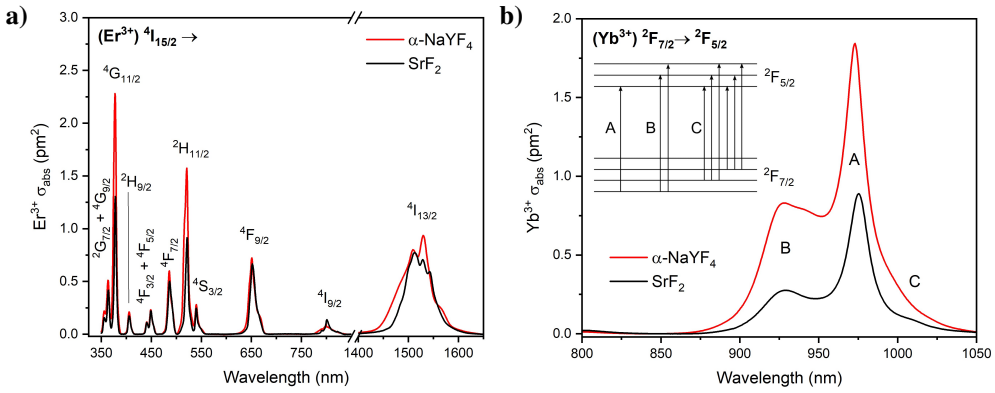


**Figure 3:** Absorption cross sections for **(a)** erbium and **(b)** ytterbium transitions from their ground states $^4I_{15/2}$ and $^2F_{7/2}$, respectively, for $SrF_2$ (*black*) and α-$NaYF_4$ (*red*) hosts. Inset shows a schematic for the crystal field splitting of the two $Yb^{3+}$ energy levels and their contribution to the spectra.

The $Yb^{3+}$:$^2F_{5/2}$ band shows three distinct spectral features originating from the possible transitions between the $^2F_{7/2}$ and $^2F_{5/2}$ manifolds (see the energy scheme in the inset of Fig. 3b). However, the $Er^{3+}$:$^4I_{11/2}$ energy level (with a rather small $\sigma_{abs}$) falls within the A-region of the $Yb^{3+}$:$^2F_5/2$ band. This resonance is required for an efficient ET between a sensitizer ($Yb^{3+}$) and activator ($Er^{3+}$) in upconverting materials. The area of the hidden $Er^{3+}$ band at around 975 nm has been estimated (method explained in Section 2.2) to calculate its experimental oscillator strength (found to be $f_{exp} = 0.94 \times 10^{-6}$ for $SrF_2$), which is in good agreement with those reported for other singly $Er^{3+}$-doped fluoride systems [16, 29].

**Table 1:** Experimental peak wavelength, its corresponding energy, experimental ($f_{exp}$, $\times 10^{-6}$) and calculated ($f_{cal}$, $\times 10^{-6}$) oscillator strengths, and their ratios ($f_{cal}/f_{exp}$), for various $Er^{3+}$ ground-state transitions in a $SrF_2$ single crystal.

| **Level $^4I_{15/2}$ →** | **λ** (nm) | **ν** ($cm^{-1}$) | $f_{exp}$ | $f_{cal}$ | $f_{cal}/f_{exp}$ |
|---|---|---|---|---|---|
| $^4I_{13/2}$ | 1511.0 | 6618.1 | 5.89 | 4.28 | 0.73 |
| $^4I_{11/2}$ | 975.5 | 10256.4 | 0.94 | 1.75 | 1.87 |
| $^4I_{9/2}$ | 801.0 | 12484.4 | 0.83 | 1.72 | 2.06 |
| $^4F_{9/2}$ | 651.5 | 15337.4 | 6.11 | 9.80 | 1.61 |
| $^4S_{3/2}$ | 539.5 | 18518.5 | 1.63 | 5.09 | 3.12 |
| $^2H_{11/2}$ | 521.5 | 19157.1 | 7.25 | 9.46 | 1.30 |
| $^4F_{7/2}$ | 486.0 | 20576.1 | 5.27 | 10.90 | 2.07 |
| $^4F_{5/2}$ | 449.0 | 22271.7 | 1.95 | 4.11 | 2.11 |
| $^4F_{3/2}$ | 441.0 | 22675.7 | 0.82 | 3.56 | 4.33 |
| $^2H_{9/2}$ | 406.0 | 24630.5 | 1.78 | 3.12 | 1.75 |
| $^4G_{11/2}$ | 378.0 | 26455.0 | 13.41 | 17.24 | 1.29 |
| $^4G_{9/2}$ | 364.0 | 27472.5 | 4.75 | 6.90 | 1.45 |
| $^2G_{7/2}$ | 356.0 | 28089.9 | 1.69 | 2.53 | 1.49 |

The experimental oscillator strengths retrieved from the $\sigma_{abs}(\lambda)$ (and the one estimated for the $^4I_{11/2}$ level) are summarized in Table 1 and compared to those calculated by means of JO theory. The ratios between the experimental and calculated $f$ values show quite big deviations in some of the cases, which may arise from the different $Er^{3+}$ site-symmetries, clustering and defects within the crystal host. For comparison, the $f_{cal}$ for $SrF_2$ and NaF are shown together with their $\sigma_{abs}$ in Fig. 4. Some of the bands shown in the absorption spectra are blue- or red-shifted in energy as compared to the calculated oscillator strengths. These shifts are attributed to different crystal field splittings caused by imperfections in the host crystals, together with the many possible ways of charge compensation for trivalent ions in cubic crystals [9], which

broaden and shift the central wavelength from their expected, infinitely narrow lines. Nevertheless, JO theory properly captures the increase in $f$ values for the $^4G_{11/2}$ and $^2H_{11/2}$ bands from $SrF_2$ to NaF. An extra transition ($^4I_{15/2} \rightarrow ^2K_{15/2}$) at *ca.* 27500 cm$^{-1}$, could not be separated due to the line broadening, is calculated to have a small $f$ but long intrinsic lifetime (see Table S3).

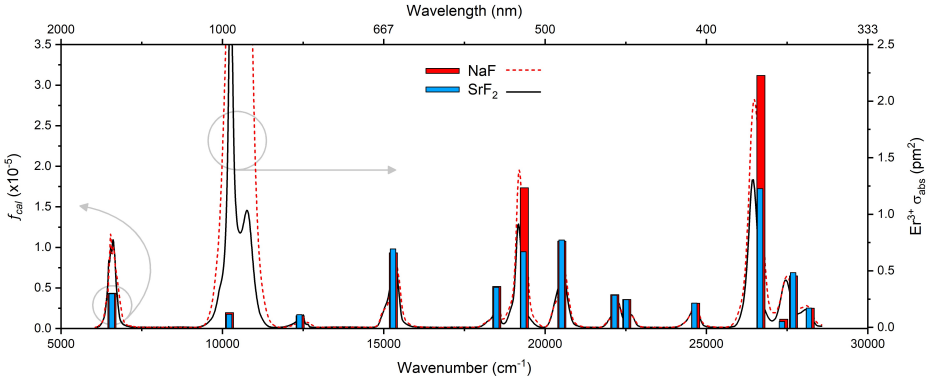


**Figure 4:** Calculated oscillator strengths (*bins; left axis*) for $Er^{3+}$ transitions in $SrF_2$ and NaF hosts, overlapped to their erbium absorption cross sections (*lines; right axis*) for comparison.

The Judd-Ofelt intensity parameters $\Omega_\lambda$ are calculated and shown in Table S1 for $SrF_2$ and NaF, as well as for other $Er^{3+}$-doped crystal hosts reported in literature. It has been shown that $\Omega_2$ parameters give an insight of the amount of covalent bonding between the dopant and host atoms, and are strongly dependent on the local environment of the ion sites, whereas the $\Omega_6$ parameter is related to the overlap integrals of the $4f$ and $5d$ orbits [13]. Values of $\Omega_4$ and $\Omega_6$ also provide some information on the hypersensitive transitions. However, compared with $\Omega_2$, which is more sensitive to the chemical nature of the hosts, structural information carried by $\Omega_4$ and $\Omega_6$ parameters is marginal and sometimes inaccurate [22]. The studied crystals show larger $\Omega_4$ and $\Omega_6$ values than other hosts reported in literature, implying an increased sensitivity of the dopants to their microenvironment and to long-range effects. The NaF host shows a large $\Omega_2$ value, which is attributed to a higher polarization and asymmetry of the RE ligands. The spectroscopic quality factor is found to be around 3 times larger in our studied hosts as compared to $CaF_2$ and β-$NaGdF_4$, indicating a lower quality of our systems which we attribute to clustering and defects. However, the oxide host ($Y_2O_3$) shows a larger $\chi$ attributed to the higher phonon energy as compared to fluorides.

### 3.1.2. Emission

The DS emissions of $Er^{3+}$ for the different crystals are shown in Fig. 5. The $^4G_{11/2}$ energy level is excited with a xenon lamp at $\lambda_{ex} = 375$ nm. The emission spectrum of a $SrF_2$ crystal is overlapped to the $\sigma_{abs}(\lambda)$ and shown in Fig. 5a. The emissions in the visible range for all the studied samples and hosts are depicted in Fig. 5b, showing a strong quenching of the blue and green emissions for the two sodium fluoride samples with higher content of $Yb^{3+}$. Interestingly, these two samples do not show the weak emission band at roughly 700 nm, of the $^2H_{9/2} \rightarrow ^4I^{11/2}$ transition. This is possibly due to the much higher probability of back energy transfer (BET) from $Er^{3+}$ to $Yb^{3+}$ in these two crystals highly loaded with $Yb^{3+}$, while populating the $^4F_{9/2}$ energy level and, thus, enhancing the red emission (see the energy level schematics of Fig. 9a). This is supported by the fact that the α-$NaYF_4$ sample with the lowest $Yb^{3+}$ content displays the highest green to red ratio among all the studied crystals, and a blue to red intensity ratio comparable to the $SrF_2$ samples, under these excitation conditions.

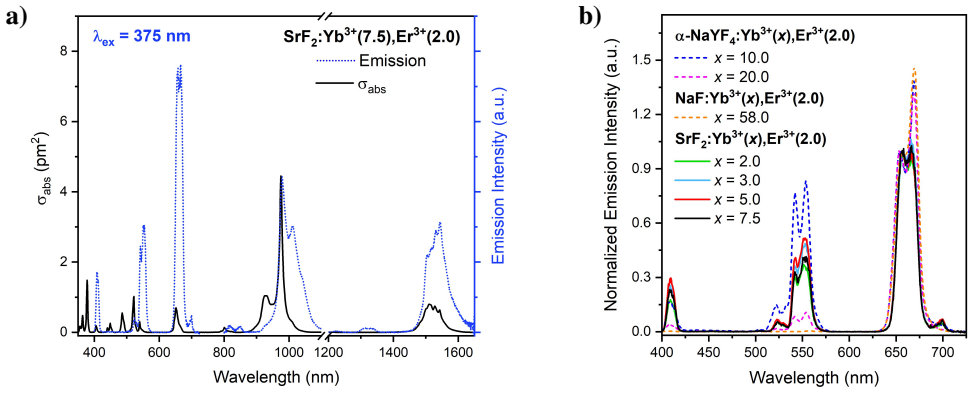


**Figure 5:** DS emission spectra under xenon lamp excitation at 375 nm; **(a)** overlapped to the erbium absorption cross sections in the visible and NIR regions for a $SrF_2$ single crystal; and **(b)** in the visible region for the $SrF_2$ (*solid lines*) and sodium fluoride (*dashed lines*) hosts, normalized to the 657 nm peak.

### 3.1.3. Decay Kinetics

The monitoring of $Yb^{3+}$:$^2F_{5/2}$ lifetime is a systematic step for all those dealing with Yb-sensitized UC materials. In terms of decay kinetics, the longer lifetimes implies a slower decay rate and hence, an accumulation of the population of this energy level [30]. The experimental lifetime values for the $Yb^{3+}$:$^2F_{5/2}$ energy level are shown in Table 2 under direct excitation of $Yb^{3+}$ with a pulsed laser diode and a μ-flash lamp at 975 nm, with similar pulse widths (∼100 μs). The discrepancies in the measured lifetimes with different excitation sources are rather small for these DS emissions. The two studied crystal hosts show an opposite behaviour regarding the evolution of the decay kinetics with their sensitizer content.

**Table 2:** Experimental radiative lifetimes of the $Yb^{3+}$:$^2F_{5/2}$ energy level for the different host crystals, measured under excitation at 976 nm with a laser diode and a μ-flash lamp. These lifetime values are obtained from single[a] and weighted averages of double[b] exponential fits.

| **Host** | **[$Yb^{3+}$], [$Er^{3+}$]** (mol%) | **$\tau_{exp}$ [$Yb^{3+}$:$^2F_{5/2}$]** (ms) Laser diode | μ-flash Lamp |
|---|---|---|---|
| $SrF_2$ | 2.0, 2.0 | 4.530[b] | 4.988[a] |
| | 3.0, 2.0 | 4.023[b] | 4.173[a] |
| | 5.0, 2.0 | 3.303[b] | 3.457[a] |
| | 7.5, 2.0 | 2.632[b] | 2.751[a] |
| α-$NaYF_4$ | 10.2, 1.8 | 0.425[a] | 0.414[a] |
| | 20.0, 2.0 | 0.102[a] | 0.095[a] |
| | 58.0, 2.0 | 0.065[a] | 0.077[a] |

Fig. 6 shows the decay curves for $SrF_2$, α-$NaYF_4$ and NaF crystals for direct excitation of $Yb^{3+}$ with a laser diode. Here, the $SrF_2$ samples clearly show a decreasing lifetime with increasing $Yb^{3+}$ concentration, while in the sodium fluoride crystals the longest lifetime is found for the sample with highest $Yb^{3+}$ content. The reason for this is expected to be the different $Yb^{3+}$-doping ranges (*i.e.* the concentration in sodium fluoride samples is above 10 mol% while in $SrF_2$ samples is under 8 mol%). A higher $Yb^{3+}$ content increases the ET rates, and so, the energy migration between $Yb^{3+}$ ions results in prolonged lifetimes in the sodium fluoride crystals. The lower sensitizer concentrations present in $SrF_2$ crystals (as compared to sodium fluorides) elongates the probed lifetimes by one order of magnitude. This is attributed to the increased distance between dopants, which decreases the ET rates (found to be proportional to $x^6$, where $x$ is the distance between donor and acceptor [5]).

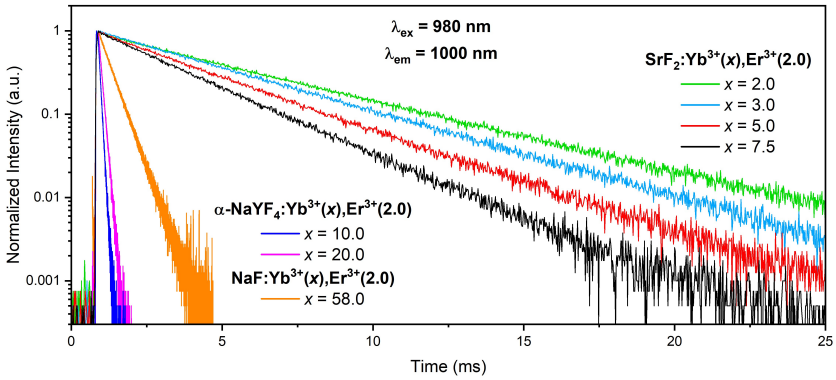


**Figure 6:** Decay kinetics of the $Yb^{3+}$:$^2F_{5/2}$ energy level for the different studied hosts, measured under laser diode excitation at 976 nm with an excitation power density of 15 W/cm$^2$.

The same experiment is performed under μ-flash lamp excitation at 375 nm (see Table 3). This table shows quite similar values of the $Yb^{3+}$:$^2F_{5/2}$ lifetimes at both excitation wavelengths, although slightly longer lifetimes are found for the excitation of high $Er^{3+}$ energy levels (at $\lambda_{ex} = 375$ nm), resulting from an ET process; while greater differences are observed for the $Er^{3+}$:$^4I_{13/2}$ band, where the experimental lifetimes are found to be longer for $\lambda_{ex} = 975$ nm. This can be explained by the fact that erbium ions are excited at 375 nm, while ytterbium ions are excited at 975 nm; hence, whenever an ET between $Er^{3+}$ and $Yb^{3+}$ ions is involved, the probed lifetime tends to increase.

**Table 3:** Experimental and calculated radiative lifetimes of $Yb^{3+}$:$^2F_{5/2}$ and $Er^{3+}$:$^4I_{13/2}$ transitions for the different samples. Experimental decay curves were measured under μ-flash lamp excitation at 375 and 975 nm, and fitted with mono-exponential decay functions.

| **Host** | **[$Yb^{3+}$], [$Er^{3+}$]** (mol%) | **$\lambda_{ex}$** (nm) | **[$Yb^{3+}$:$^2F_{5/2}$]** **$\tau_{exp}$** (ms) | **[$Er^{3+}$:$^4I_{13/2}$]** **$\tau_{exp}$** (ms) | **$\tau_{cal}$** (ms) |
|---|---|---|---|---|---|
| $SrF_2$ | 2.0, 2.0 | 375 | 5.109 | 14.925 | 3.96 |
| | | 975 | 4.988 | 17.407 | 3.96 |
| | 7.5, 2.0 | 375 | 2.799 | 11.722 | 3.96 |
| | | 975 | 2.751 | 12.825 | 3.96 |
| α-$NaYF_4$ | 10.2, 1.8 | 375 | 0.443 | 7.940 | 3.89 |
| | | 975 | 0.414 | 7.896 | 3.89 |
| | 20.0, 2.0 | 375 | 0.156 | 5.857 | 3.89 |
| | | 975 | 0.095 | 5.909 | 3.89 |
| | 58.0, 2.0 | 375 | 0.126 | 6.624 | 3.89 |
| | | 975 | 0.077 | 6.716 | 3.89 |

## *3.2. Upconversion Properties*

### 3.2.1. Decay Kinetics

The decay kinetics for the green and red UC emissions are studied in the different crystal hosts ($SrF_2$ and $NaYF_4$) under laser diode excitation at 976 nm, as shown in Fig. 7. For the green emission, double and triple exponential decay functions are used to fit the experimental data. The short and long lifetime components are clearly visible in the decay data (Fig. 7a), where the $SrF_2$ samples show faster and slower decay components (*e.g.* multiple exponential fits are used) for lower sensitizer doping. The fast decays are attributed to the intrinsic $Er^{3+}$ lifetimes (see Table S2), while the long decays are related to the slow ET processes between the ions in the crystal matrix, increasing the probed lifetimes. For the red emission (Fig. 7b), the decay times

decrease monotonically with $Yb^{3+}$ concentration. However, rise times increase continuously with $Yb^{3+}$ concentration. The $NaYF_4$ samples show faster rise and decay times for both, green and red UC emissions, with same trends as described for $Yb^{3+}$ lifetimes in Section 3.1.3.

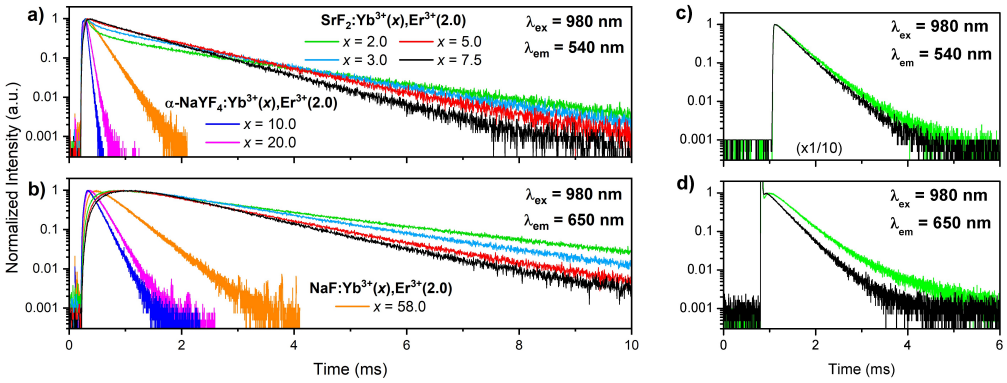


**Figure 7:** Decay kinetics of the **(a, c)** $Er^{3+}$:$^2H_{11/2}$,$^4S_{3/2}$, and **(b, d)** $Er^{3+}$:$^4F_{9/2}$ energy levels for the studied crystals under **(a, b)** laser diode and **(c, d)** μ-flash lamp excitation at 976 nm.

The experimental and calculated lifetimes for the green and red UC emissions under laser diode and μ-flash lamp excitation at 976 nm for $SrF_2$ and $NaYF_4$ are presented in Table S2. Here, we observe increased experimental lifetime values of the green emission in $SrF_2$ crystals for increased $Yb^{3+}$ concentrations. This is attributed the contribution of the fast decays in the weighted averages of the different lifetime components. Note the differences of around one order of magnitude observed when measuring lifetimes with different light sources (Fig. 7a,c and 7b,d). This is clearly due to the different excitation power density of the two lamps (*e.g.* the increased power density elongates the probed lifetime by enhancing populations). The decay kinetics were also studied at different excitation wavelengths under μ-flash lamp excitation (low *P*), without yielding significant differences in the measured lifetimes. Therefore, we conclude that the excitation power density (rather than the wavelength) plays a major role in elongating the decay kinetics of UC emissions.

### 3.2.2. Population Pathways

The population pathways were investigated by means of excitation scans for the downshifted emissions at 542, 655 and 980 nm. These are presented in Figs. 8, 9 and 10 together with the energy schemes showing some of the corresponding pathways for the population of the emitting states. Here, the excitation wavelength is scanned while the intensity at a fixed emission wavelength is probed. The resulting spectra relates the photons absorbed at each wavelength with the photons emitted from a single excited state, which provides information about the population pathways of the probed energy levels.

As shown in Fig. 8, there are no significant differences in the emission intensities of the $Er^{3+}$:$^4S_{3/2}$ band for varying concentrations of $Yb^{3+}$ in the $SrF_2$ single crystals. However, Fig. 9 shows a decrease in the emission intensity of the $^4F_{9/2}$ energy level at short excitation wavelengths for the samples with lower $Yb^{3+}$ content. This implies a better coupling between the $^4F_{9/2}$ and the higher energy levels for crystals with higher $Yb^{3+}$ concentrations. This is explained by the fact that the most efficient way to populate the $^4F_{9/2}$ manifold is via a BET from $Er^{3+}$ to $Yb^{3+}$ (shown in Fig. 9a), the probability of which is enhanced at higher $Yb^{3+}$ content.

Another pathway for the population of the $^4F_{9/2}$ energy level of $Er^{3+}$ is the non-radiative relaxation from the $^2H_{11/2}$ states, which is as efficient as the BET depicted in Fig. 9a at low

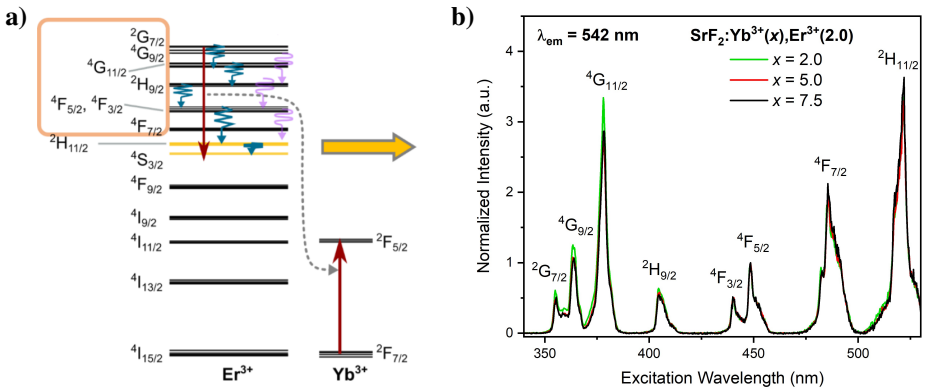


**Figure 8: (a)** Energy level scheme (modified from Fig. S11, [11]) showing some non-radiative pathways for the population of the $Er^{3+}$:$^4S_{3/2}$ energy level probed by means of **(b)** the excitation spectra measured for the 542 nm emission, normalized to the $^4F_{5/2}$ peak.

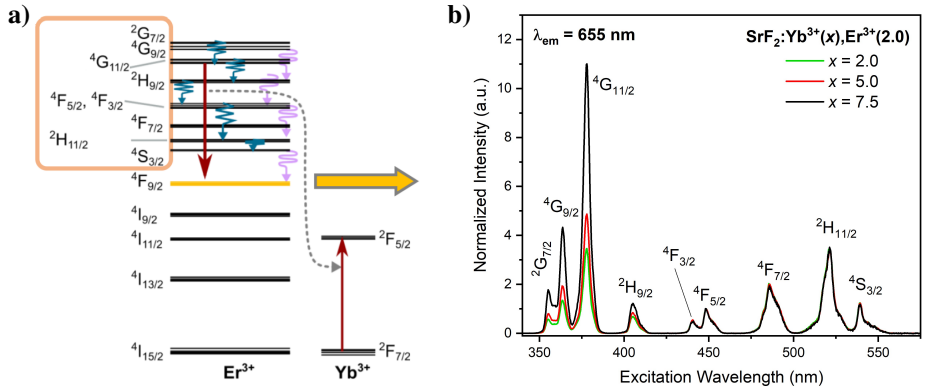


**Figure 9: (a)** Energy level scheme (modified from Fig. S12, [11]) showing some non-radiative pathways for the population of the $Er^{3+}$:$^4F_{9/2}$ energy level probed by means of **(b)** the excitation spectra obtained for the 655 nm emission, normalized to the $^4F_{5/2}$ peak.

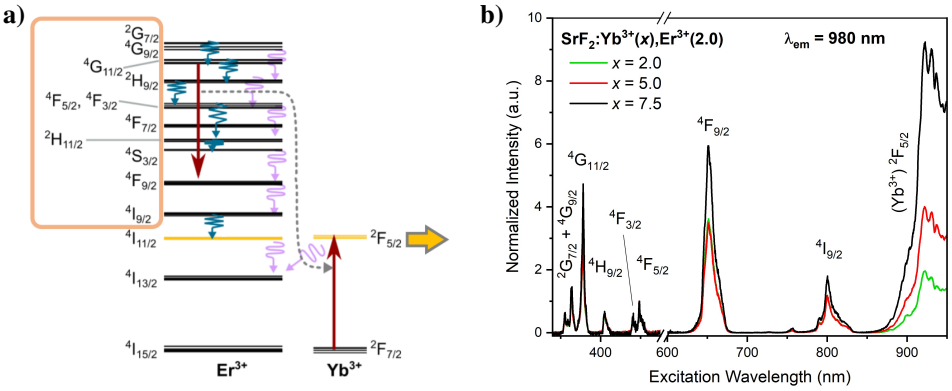


**Figure 10: (a)** Energy level scheme (modified from Fig. S13, [11]) showing some non-radiative pathways for the population of the $Er^{3+}$:$^4I_{11/2}$ and the $Yb^{3+}$:$^2F_{5/2}$ energy levels probed by means of **(b)** the excitation spectra recorded at an emission wavelength of 980 nm, normalized to the $^4F_{5/2}$ peak.

sensitizer concentration. On the other hand, we observed strong emission from the $Yb^{3+}$:$^2F_{5/2}$ energy level at 980 nm when the $Er^{3+}$:$^4G_{11/2}$ energy level is pumped (Fig. 10b). This is an indication that an BET process populates the $Yb^{3+}$:$^2F_{5/2}$ and the $Er^{3+}$:$^4F_{9/2}$ energy levels as shown in the energy level diagram of Fig. 10a. Nevertheless, these ETs from the high energy levels of $Er^{3+}$ seem not to depend on the $Yb^{3+}$ concentration. The $^4F_{9/2}$ and $^4I_{9/2}$ energy levels of $Er^{3+}$ show a better coupling to the 980 nm emission for the $SrF_2$ crystal with highest $Yb^{3+}$ concentration. In the case of direct excitation of the $Yb^{3+}$:$^2F_{5/2}$ energy level, we expectedly observe a monotonic increase in the 980 nm emission for increasing $Yb^{3+}$ doping.

### 3.2.3. Upconversion Emission

The UC emissions of the $SrF_2$ and $NaYF_4$ single crystals are measured under laser diode excitation at 976 nm (and compared to those obtained under xenon lamp excitation at 375 nm for the $SrF_2$ samples), and shown in Fig. 11. For the $NaYF_4$ samples, smaller green to red intensity ratios (as opposed to those observed for DS emissions in Fig. 5b), and very week intensities for the $^4S_{3/2} \rightarrow ^4I_{13/2}$ transition at *ca.* 850 nm, are found. The effect of the host matrix is observed in the increased intensity of the peak centered at around 675 nm of the red band, which originates from the different crystal field splitting between $SrF_2$ and $NaYF_4$. Again, we can see the strong enhancement of the red UC emission in $NaYF_4$ due to the higher $Yb^{3+}$ concentrations in these samples, which is responsible for an increased population of the $^2F_{5/2}$ energy level *via* BET from $Er^{3+}$ to $Yb^{3+}$ (suggested in Fig. 9a). From the comparison between the UC and DS emissions (Fig. 11b) we can observe two features: (*i*) the sensitizer concentration plays an important role in the intensity ratios of different UC emission bands, due to the complex ET processes between the $Yb^{3+}$ and $Er^{3+}$ ions in the crystal matrix; and (*ii*) the emissions from the $^2H_{9/2}$ energy level to the $^4I_{11/2}$ and $^4I_{9/2}$ are only found for short excitation wavelengths (375 nm), because the high energy levels are more efficiently populated when using short wavelengths (375 nm; DS emission) as compared to long wavelengths (975 nm; UC emission), which require from ET processes.

The *P*-dependent UC emission spectra recorded with an integrating sphere setup (described in Section 2) is shown for a $SrF_2$ single crystal in Fig. 12. Here, the different bands are rescaled for better comparison to the red emission. From such spectra, the *P*-dependent slope factors ($k$), intensity ratios ($I_{b/g}$, $I_{g/g}$ and $I_{g/r}$) and upconversion quantum yields ($\Phi_{UC}$) are calculated for the $SrF_2$ emission bands in the visible region of the spectra.

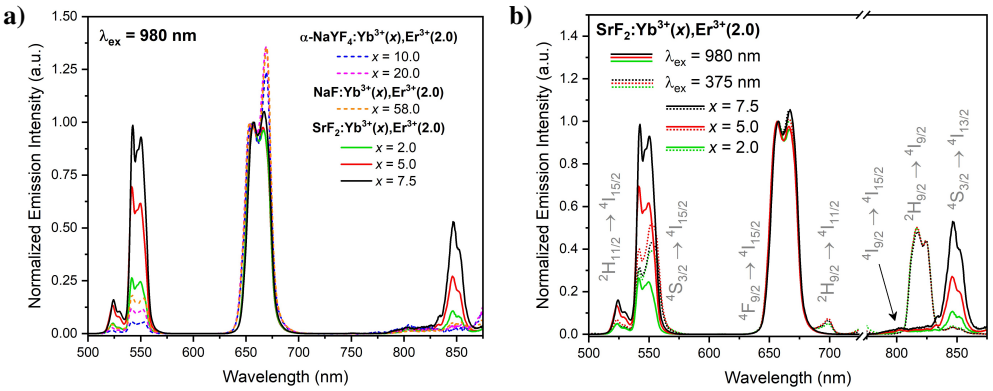


**Figure 11:** UC emission spectra under laser diode excitation at 976 nm **(a)** for the $SrF_2$ (*solid lines*) and $NaYF_4$ (*dashed lines*) hosts; and **(b)** overlapped to the DS emission obtained under Xe lamp excitation at 375 nm (*dotted lines*) for the $SrF_2$ crystals. Both, UC and DS emissions are normalized to 657 nm.

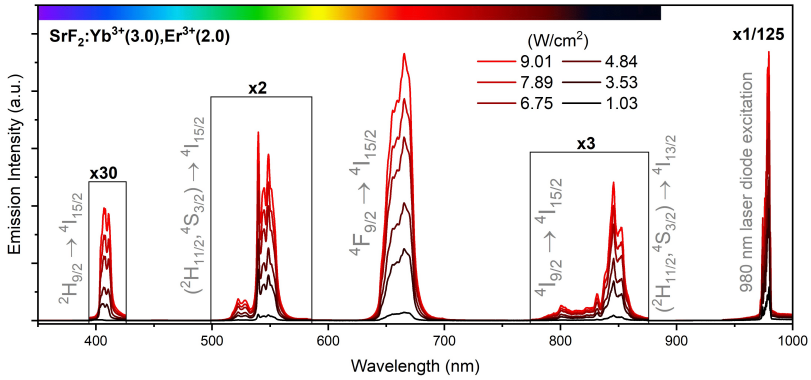


**Figure 12:** UC emission spectra for a $SrF_2$ crystal under laser diode excitation at 976 nm with varying excitation power densities. The color code relates the wavelength to the emission color of each band.

The $P$-dependent slope factors ($k(P)$) of the blue, green and red UC emissions for $SrF_2$ are summarized in Fig. 13. In the low, unsaturated $P$ regime, $k$ values of the blue emissions are the highest and provide the number of photons required for the generation of each emission band ($I_{UC} \sim P^k$). With increasing $P$, $k(P)$ decreases as a consequence of the enhanced population and onset of saturation of the different emissive states of the $Er^{3+}$ ions, thus approaching a value of $k = 1$. This suggests that the energy levels responsible for the green ($^4S_{3/2}$) and red ($^4F_{9/2}$) emissions are close to saturation (*e.g.* lower energy levels are already populated and thus only one photon is needed to promote an electron) at around 10 W/cm$^2$. Although it has been shown that the $^4F_{9/2}$ energy level populates from 2 or 3 photonic processes in $Er^{3+}$, $Yb^{3+}$ nanoparticles [11], there is no evidence from the estimated slope factors that 3-photonic processes occur in the investigated $SrF_2$ single crystals (see Fig. 9).

The blue to green, green to green and green to red intensity ratios for $SrF_2$ under laser diode excitation at 976 nm are shown in Fig. 14. Here, we observe an increase by a factor of 3 for $I_{b/g}$ from 1 to 9 W/cm$^2$ (note that this parameter is around one order of magnitude larger for the blue DS emission shown in Fig. 5). As the blue UC emission is a 3-photon process, at higher excitation power densities the blue UC emission is enhanced. The $I_{g/g}$ are temperature indicators, as the energy difference is rather small (~600 cm$^{-1}$), and population follows a Boltzmann

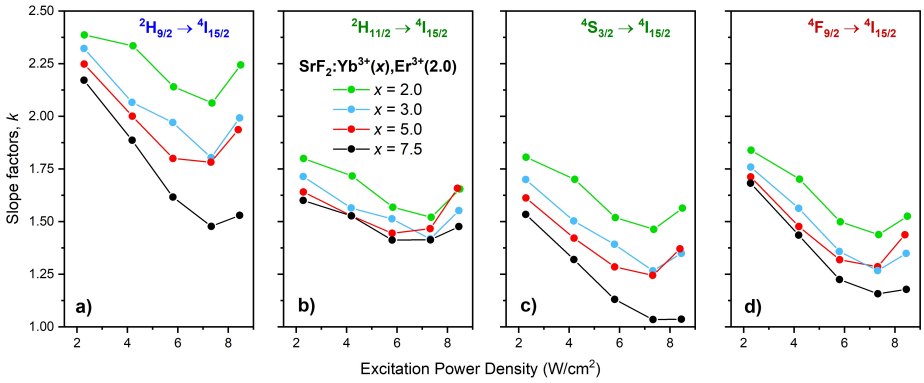


**Figure 13:** $P$-dependent slope factors of the (a) blue, (b,c) green and (d) red bands for the upconversion emissions of the $SrF_2$ single crystals.

distribution. At higher temperatures the population of the upper level ($^2H_{11/2}$) increases. The higher content of $Yb^{3+}$ increases the absorption at 976 nm and, therefore, the heating effects.

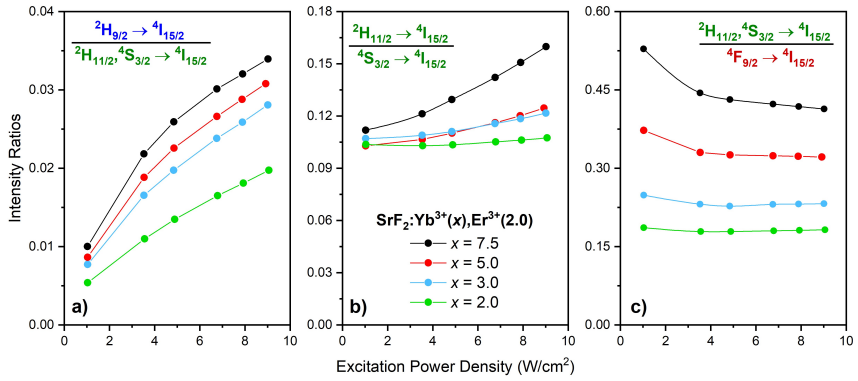


**Figure 14:** **(a)** Blue to green ($I_{b/g}$), **(b)** green to green ($I_{g/g}$), and **(c)** green to red ($I_{g/r}$) *P*-dependent intensity ratios for the UC emissions of the $SrF_2$ single crystals under laser diode excitation at 976 nm.

The $\Phi_{UC}$ measurements are corrected for $Yb^{3+}$ emission, as there is a resonance between the excitation laser line and the broad $Yb^{3+}$ emission at 980 nm which otherwise leads to an overestimation of $\Phi_{UC}$. The corrected values of the *P*-dependent absolute UC quantum yields, $\Phi_{UC}$, for the visible emissions in $SrF_2$ matrix are presented in Fig. 15. Here, we observe an increase in the efficiency of the blue and green UC emissions at higher $Yb^{3+}$ concentrations, while the opposite is found for the red band. In any case, the quantum yield values increase with excitation power density.

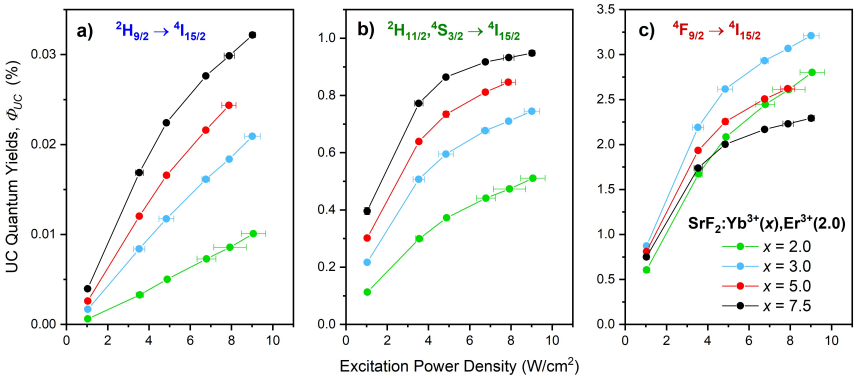


**Figure 15:** *P*-dependent absolute $\Phi_{UC}$ for the **(a)** blue, **(b)** green and **(c)** red upconversion emissions of the $SrF_2$ single crystals.

## 4. Conclusion and Outlook

In this work, we spectroscopically characterized a series of $Er^{3+}$, $Yb^{3+}$ co-doped fluoride single crystals in three different hosts, $SrF_2$, $\alpha$-$NaYF_4$ and NaF. Their optical properties have been studied by means of absorption, luminescence, decay kinetics and excitation spectra, and compared to those found by implementing the Judd-Ofelt theory for ideal, singly Er-doped $SrF_2$ and $NaYF_4$ hosts. The emission properties have been studied as a function of the excitation wavelength and power density, and an extensive analysis of the UC emission was carried

out to obtain the *P*-dependent parameters derived from the NIR to visible upconversion emission from the doubly doped $SrF_2$ single crystals. The *P*-dependence, sensitizer concentration or crystal symmetry are not taken into account by the Judd-Ofelt theory, all of which play an important role in the probed properties of the $Er^{3+}$, $Yb^{3+}$ co-doped systems. This is in part a limitation of the theory to predict the UC properties beforehand.

This extensive collection of spectroscopic data will provide a solid basis to compare the performance of nanoscale systems with the same hosts and dopants. From these studies we conclude that high sensitizer concentrations lead to crystal defects and RE clustering, resulting in shorter decays and inefficient UC emission. We found no evidence of 3-photonic population of the red-emitting level, as compared to the most efficient NPs [11] (this processes dominate at high *P*). We found comparably high $\Phi_{UC}$ in the low *P* range compared to UCNPs and long $Yb^{3+}$ lifetime for moderately low doped systems.

However, some more experiments would be useful to completely characterize the studied samples, such as inductive coupled plasma mass spectroscopy (ICP-MS) to properly characterize the dopant concentration (*e.g.* the concentrations given in this work are estimates from the growth procedure), or X-ray diffraction (XRD) studies to characterize crystal structure of the hosts. Furthermore, the homogeneity of the dopants within the crystal rods should be checked by local-XRD.

# Supplementary Information

**Table S1:** Judd-Ofelt intensity parameters ($\Omega_\lambda$, $\times 10^{-20}$ $cm^2$) and spectroscopic quality factor ($\chi = \Omega_4/\Omega_6$) for the crystals studied in the present work and other reported $Er^{3+}$-doped systems.

| **Host** | $\Omega_2$ | $\Omega_4$ | $\Omega_6$ | $\chi = \Omega_4/\Omega_6$ |
|---|---|---|---|---|
| $SrF_2$ | 2.36 | 5.55 | 3.58 | 1.55 |
| NaF | 7.53 | 5.07 | 3.62 | 1.40 |
| $CaF_2$ [15] | 1.13 | 0.94 | 1.82 | 0.51 |
| $Y_2O_3$ [14] | 4.59 | 1.21 | 0.48 | 2.52 |
| β-$NaGdF_4$ [18] | 4.97 | 1.16 | 2.03 | 0.57 |

**Table S2:** Experimental and calculated radiative lifetimes of two $Er^{3+}$ transitions using different excitation sources at 976 nm for the different host crystals. Experimental lifetime values are obtained from weighted averages of single[a], double[b] and triple[c] exponential decay functions.

| **Host** | **Exc. Source** | **[$Yb^{3+}$], [$Er^{3+}$]** (mol%) | **[$Er^{3+}$:$^2H_{11/2}$,$^4S_{3/2}$]** $\tau_{exp}$ (ms) | $\tau_{cal}$ (ms) | **[$Er^{3+}$:$^4F_{9/2}$]** $\tau_{exp}$ (ms) | $\tau_{cal}$ (ms) |
|---|---|---|---|---|---|---|
| $SrF_2$ | Laser diode | 2.0, 2.0 | 0.183[c] | 0.18, 0.28 | 2.180[b] | 0.29 |
| | | 3.0, 2.0 | 0.351[c] | 0.18, 0.28 | 1.814[b] | 0.29 |
| | | 5.0, 2.0 | 0.908[b] | 0.18, 0.28 | 1.499[b] | 0.29 |
| | | 7.5, 2.0 | 0.991[b] | 0.18, 0.28 | 1.217[b] | 0.29 |
| | μ-flash lamp | 2.0, 2.0 | 0.042[a] | 0.18, 0.28 | 0.417[b] | 0.29 |
| | | 5.0, 2.0 | 0.039[a] | 0.18, 0.28 | 0.374[a] | 0.29 |
| | | 7.5, 2.0 | 0.038[a] | 0.18, 0.28 | 0.352[b] | 0.29 |
| $NaYF_4$ | Laser diode | 10.2, 1.8 | 0.206[a] | 0.10, 0.27 | 0.394[a] | 0.30 |
| | | 20.0, 2.0 | 0.188[a] | 0.10, 0.27 | 0.183[a] | 0.30 |
| | | 58.0, 2.0 | 0.033[a] | 0.10, 0.27 | 0.159[a] | 0.30 |
| | μ-flash lamp | 10.2, 1.8 | 0.028[b] | 0.10, 0.27 | 0.164[a] | 0.30 |
| | | 20.0, 2.0 | 0.015[b] | 0.10, 0.27 | 0.005[a] | 0.30 |
| | | 58.0, 2.0 | 0.005[a] | 0.10, 0.27 | 0.004[a] | 0.30 |

**Table S3:** Emission transitions (SLJ → S'L'J'), calculated wavelengths ($\lambda$, nm) and corresponding energies ($\nu$, $cm^{-1}$), derived spontaneous emission rates ($A$, $s^{-1}$), branching ratios ($\beta_R$, %) and radiative lifetimes ($\tau_R$, ms) for some excited states of $Er^{3+}$ ions in $SrF_2$ host. Only those transitions within the 300-1700 nm range with $\beta_R > 1$ % are shown.

| ***SLJ*** | ***S'L'J'*** | $\lambda$ (nm) | $\nu$ ($cm^{-1}$) | $A$ ($s^{-1}$) | $\beta_R$ (%) | $\tau_R$ (ms) |
|---|---|---|---|---|---|---|
| $^4I_{13/2} \rightarrow$ | $^4I_{15/2}$ | 1521.9 | 6570.9 | 252.36 | 100.00 | 3.960 |
| $^4I_{11/2} \rightarrow$ | $^4I_{15/2}$ | 979.7 | 10206.9 | 250.50 | 85.30 | 3.410 |
| $^4I_{9/2} \rightarrow$ | $^4I_{15/2}$ | 807.4 | 12386.2 | 361.42 | 78.43 | 2.170 |
| $^4F_{9/2} \rightarrow$ | $^4I_{15/2}$ | 654.1 | 15287.4 | 3153.74 | 92.14 | 0.292 |
| | $^4I_{13/2}$ | 1147.2 | 8716.5 | 141.50 | 4.13 | |
| $^4S_{3/2} \rightarrow$ | $^4I_{15/2}$ | 540.9 | 18488.9 | 2403.50 | 66.41 | 0.276 |
| | $^4I_{13/2}$ | 839.1 | 11918.0 | 993.10 | 27.44 | |
| | $^4I_{11/2}$ | 1207.4 | 8282.0 | 77.44 | 2.14 | |
| | $^4I_{9/2}$ | 1638.6 | 6102.7 | 143.94 | 3.98 | |
| $^2H_{11/2} \rightarrow$ | $^4I_{15/2}$ | 517.4 | 19328.0 | 4887.50 | 88.72 | 0.182 |
| | $^4I_{13/2}$ | 783.9 | 12757.1 | 243.24 | 4.42 | |
| | $^4I_{11/2}$ | 1096.4 | 9121.1 | 267.40 | 4.85 | |
| | $^4I_{9/2}$ | 1440.5 | 6941.8 | 100.33 | 1.82 | |
| $^4F_{7/2} \rightarrow$ | $^4I_{15/2}$ | 487.5 | 20512.6 | 6355.75 | 75.88 | 0.119 |
| | $^4I_{13/2}$ | 717.3 | 13941.7 | 1206.68 | 14.41 | |
| | $^4I_{11/2}$ | 970.3 | 10305.7 | 523.04 | 6.24 | |
| | $^4I_{9/2}$ | 1230.6 | 8126.4 | 273.21 | 3.26 | |
| $^4F_{5/2} \rightarrow$ | $^4I_{15/2}$ | 451.4 | 22150.9 | 2798.74 | 44.91 | 0.160 |
| | $^4I_{13/2}$ | 641.8 | 15580.0 | 2657.48 | 42.64 | |
| | $^4I_{11/2}$ | 837.24 | 11944.0 | 292.93 | 4.70 | |
| | $^4I_{9/2}$ | 1024.1 | 9764.7 | 209.04 | 3.35 | |
| | $^4F_{9/2}$ | 1457.0 | 6863.5 | 264.68 | 4.25 | |
| $^4F_{3/2} \rightarrow$ | $^4I_{15/2}$ | 444.1 | 22516.6 | 2508.69 | 45.53 | 0.181 |
| | $^4I_{13/2}$ | 627.1 | 15945.7 | 240.07 | 4.36 | |
| | $^4I_{11/2}$ | 812.4 | 12309.7 | 1992.72 | 36.17 | |
| | $^4I_{9/2}$ | 987.1 | 10130.4 | 723.22 | 13.13 | |
| $^2H_{9/2} \rightarrow$ | $^4I_{15/2}$ | 406.1 | 24626.9 | 2640.42 | 31.97 | 0.121 |
| | $^4I_{13/2}$ | 553.8 | 18056.0 | 2349.24 | 28.44 | |
| | $^4I_{11/2}$ | 693.5 | 14420.0 | 585.14 | 7.08 | |
| | $^4I_{9/2}$ | 816.9 | 12240.7 | 2400.12 | 29.06 | |
| | $^4F_{9/2}$ | 1070.7 | 9339.5 | 238.12 | 2.88 | |
| $^4G_{11/2} \rightarrow$ | $^4I_{15/2}$ | 375.1 | 26661.0 | 17153.25 | 72.61 | 0.042 |
| | $^4I_{13/2}$ | 497.8 | 20090.1 | 3473.06 | 14.70 | |
| | $^4I_{11/2}$ | 607.8 | 16454.1 | 1959.26 | 8.29 | |
| | $^4F_{9/2}$ | 879.2 | 11373.6 | 298.02 | 1.26 | |
| | $^2H_{11/2}$ | 1363.7 | 7333.0 | 469.16 | 1.99 | |
| $^2K_{15/2} \rightarrow$ | $^4I_{15/2}$ | 365.8 | 27338.5 | 906.32 | 34.09 | 0.376 |
| | $^4I_{13/2}$ | 481.5 | 20767.6 | 127.54 | 4.80 | |
| | $^4I_{11/2}$ | 583.7 | 17131.6 | 611.99 | 23.02 | |
| | $^4I_{9/2}$ | 668.8 | 14952.3 | 636.52 | 23.94 | |
| | $^4F_{9/2}$ | 829.8 | 12051.1 | 96.72 | 3.64 | |
| | $^2H_{11/2}$ | 1248.4 | 8010.5 | 266.37 | 10.02 | |
| $^4G_{9/2} \rightarrow$ | $^4I_{15/2}$ | 361.2 | 27685.3 | 7412.48 | 38.66 | 0.052 |
| | $^4I_{13/2}$ | 473.6 | 21114.3 | 8355.69 | 43.58 | |
| | $^4I_{11/2}$ | 572.1 | 17478.3 | 1148.80 | 5.99 | |
| | $^4I_{9/2}$ | 653.6 | 15299.0 | 300.99 | 1.57 | |
| | $^4F_{9/2}$ | 806.6 | 12397.8 | 1316.34 | 6.87 | |
| | $^2H_{11/2}$ | 1196.6 | 8357.3 | 298.42 | 1.56 | |
| $^4G_{7/2} \rightarrow$ | $^4I_{15/2}$ | 354.9 | 28177.2 | 2817.10 | 22.37 | 0.079 |
| | $^4I_{13/2}$ | 462.8 | 21606.3 | 1623.17 | 12.89 | |
| | $^4I_{11/2}$ | 556.5 | 17970.3 | 4533.83 | 36.00 | |
| | $^4I_{9/2}$ | 633.3 | 15791.0 | 2956.18 | 23.47 | |
| | $^4S_{3/2}$ | 1032.2 | 9688.3 | 208.45 | 1.65 | |
| | $^2H_{11/2}$ | 1130.0 | 8849.2 | 189.76 | 1.51 | |
| | $^4F_{7/2}$ | 1304.7 | 7664.6 | 148.03 | 1.18 | |